Multiphysics coupled optimization and radiation analysis of a pentamode matching layer for airborne electromagnetic pulse acoustic sources

WANG Jinge[1] SUN Zhaoyong[1,2†] TIAN Yimin[1] JI Peifeng[3†] YANG Jun[2,3]

1 Beijing Institute of Graphic Communication, Beijing 102600, China
2 State Key Laboratory of Acoustics and Marine Information, Beijing 100190, China
3 Institute of Acoustics, Chinese Academy of Sciences, Beijing 100190, China

Received December 6, 2025; accepted March 11, 2026

Abstract Airborne electromagnetic pulse acoustic sources face a severe impedance mismatch, causing low energy transmission efficiency. This work proposes a pentamode matching layer design using multiphysics coupling. We develop a finite element model integrating circuit, electromagnetic, structural, and acoustic fields, and employ a genetic algorithm to optimize matching layer parameters. Results demonstrate that the optimized pentamode layer significantly increases peak sound pressure and reconfigures resonance frequencies with new band peaks. Analysis reveals an inertial-cavity coupling effect between layer and plate that enhances both high- and low-frequency radiation, improving radiation intensity, spatial directivity, and electromagnetic-acoustic conversion efficiency. This study provides a new theoretical basis and structural design approach for efficient radiation of electromagnetic pulse acoustic sources in air, and it has important scientific significance and engineering application prospects.

Keywords Electromagnetic pulse acoustic source, Pentamode metamaterials, Impedance matching layer, Optimization algorithm

PACS: 43.20, 43.38, 43.40 **DOI:** 10.3724/0217-9776.2025009 **CSTR:** 32050.14.11-2066.2025009

1 Introduction

The electromagnetic pulse acoustic source (boomer) was first proposed by Edgerton[1]. Owing to its characteristics of high power, short pulse, and broad frequency band, it has significant application value in marine and seismic exploration[1-5] as well as geological surveying[6], and has seen continuous development.

Early researchers greatly enhanced its performance through work on finite element modeling[7] and the development of high-energy sound sources[8-15], which propelled its use in marine seismic exploration. For example, Feng *et al*.[16] explored the complementarity of parametric array profiling and spark source profiling for shallow sub-bottom surveys, providing a new method for integrated marine geological investigation. Xie *et al*.[17] used simulations and experiments to investigate the potential application of a deep-sea pulse sound source based on high-power electromagnetic pulse principles for deep-sea exploration. Vesnaver and Baradello[18] proposed a workflow for processing single-channel chirp and boomer survey data, which can effectively process and analyze seismic data and provides a new method for high-resolution imaging of seabed strata. Gao *et al*.[19] focused on electromagnetic pulse sound sources generated by high-voltage discharges in fluids, experimentally and numerically comparing the discharge characteristics of various electrode configurations, thereby providing experimental evidence and design foundations for optimizing source performance. Building on this, Du *et al*.[20] verified the feasibility of achieving a high sound pressure level output with a low-power electromagnetic pulse source, offering an important technological pathway for developing efficient electromagnetic pulse sources. Jiang *et al*.[21] proposed a deep-sea broadband electromagnetic pulse source technology based

This work was supported by the Beijing Institute of Graphic Communication Projects (BIGC Ea202511), the National Medical Products Administration Key Laboratory for Quality Evaluation of Ultrasonic Surgical Equipment (KF202501), the State Key Laboratory of Acoustics and Marine Information, Chinese Academy of Sciences (SKLA202517) and the Beijing Natural Science Foundation (1262043).
† Corresponding author: SUN Zhaoyong, sunzhaoyong@bigc.edu; JI Peifeng, jipeifeng@mail.ioa.ac.cn

© The Author(s) 2026. This is an open access article under the CC-BY 4.0 License (https://creativecommons.org/licenses/by/4.0/).

on pressure-compensation balancing, which offers guidance for operating electromagnetic pulse sources in high-pressure deep-sea environments. Furthermore, Velikhov and Panchenko[22] expanded the engineering development of high-power electromagnetic pulse technology, providing key support for deep-sea electromagnetic pulse source research and development; they systematically demonstrated the feasibility of using a self-contained magnetohydrodynamic device to generate high-power electromagnetic pulses, marking an important step in advancing electromagnetic pulse source technology from principle to engineering implementation.

The boomer's attributes of high sound pressure, high power, and short pulse also give it potential for use in air, such as for bird dispersal or bio-interference. However, although this source technology is relatively mature in underwater environments, expanding its use into the air faces significant engineering obstacles and acoustic challenges. The biggest problem is the huge acoustic impedance difference between the vibrating emitting plate and air, which causes most acoustic energy to be reflected when coupling from solid to air. The conversion efficiency from electromagnetic to acoustic energy is extremely low, severely limiting the source's output performance. At present, research on the impedance matching problem for electromagnetic pulse sources radiating in air is very limited, and effective improvement approaches are lacking. Impedance matching layer technology is an important means to solve this problem. By adding a specially designed impedance matching medium between the plate and air, the impedance transition can be smoothed, and energy reflection can be reduced[23-25]. Considering that a matching layer might also face solid-solid and solid-air coupling issues (for instance, shear-mode resonance in the layer could negatively affect its performance), we consider using a pentamode artificial material structure as the matching medium to mitigate the impact of shear wave resonances. In a pentamode material, of the six eigenvalues of the elastic stiffness tensor, only one is non-zero (corresponding to a pure compression mode) while the other five eigenmodes have nearly zero shear stiffness. Thus, mechanically, this material behaves like a fluid but with a designed structural form[26-29]. This characteristic gives pentamode materials superior capabilities in manipulating sound waves, and considerable progress has been made in recent years[30-41]. By introducing a pentamode material as the matching layer, compressional waves can be transmitted effectively while the influence of shear waves is suppressed, thereby maximizing the radiation efficiency of the plate's vibration into airborne sound.

In this work, a multiphysics finite element model of the electromagnetic pulse acoustic source was constructed, taking into account the coupled effects of the discharge circuit, electromagnetic force, plate elastic vibration, and sound field propagation, to simulate the source's transient radiation behavior in air. On this basis, initial matching layer parameters were determined according to the classic quarter wavelength theory, and a genetic algorithm (GA) was further employed to optimize the pentamode material microstructure's key parameter combination to maximize the sound pressure output. Simulation results show that the designed impedance matching layer significantly improves the acoustic radiation ability of the electromagnetic pulse source: compared to the no-layer case, the peak sound pressure of the source with the optimized matching layer is greatly increased, the sound field wavefront becomes more continuous and regular, and axial energy concentration is clearly improved. The proposed matching layer design method provides a useful reference for addressing the energy coupling efficiency problem of electromagnetic acoustic sources in air, and it can also offer insights for structural optimization of other types of pulse sound sources.

2 Finite element simulation of the electromagnetic pulse sound source

The electromagnetic pulse acoustic source mainly consists of a capacitor, a switch, a disk-shaped (pancake) coil, and a metal emitting plate. Its basic working principle is shown in Fig. 1. When the capacitor discharges, the current passing through the pancake coil produces an instantaneous pulsed magnetic field; by electromagnetic induction, an eddy current is excited in the metal plate located above the coil. This eddy current, under the magnetic field, experiences a Lorentz force forming a strong axial repulsive electromagnetic force, which drives the metal plate into elastic vibration and radiates a pulsed sound wave outward through coupling with the surrounding medium.

To accurately analyze the operating mechanism of the electromagnetic pulse source, a finite element model encompassing multiple coupled physical domains (i.e., circuit, magnetic field, solid mechanics, and pressure acoustics) was established using COMSOL Multiphysics. Considering that both the emitting plate and the pancake coil are axially

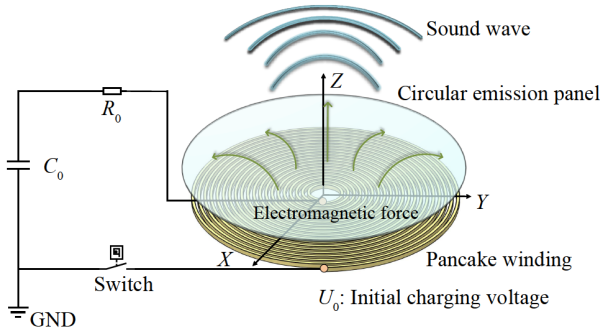


Fig. 1 Conceptual diagram of airborne electromagnetic pulse sound source.

symmetric structures, the model is built in a two-dimensional (2D) axisymmetric configuration, with geometric dimensions of 170 mm × 1050 mm, as shown in Fig. 2. Except for the boundary along the symmetry axis, the other three boundaries are set as plane wave radiation boundary conditions to simulate an open air domain. In terms of layout, the pancake coil is positioned below the metal emitting plate with a gap of 1 mm. The coil has a total of 27 turns composed of a set of tightly packed rectangular wires (each wire has a rectangular cross-section); the coil's inner radius is 32.5 mm, and its outer radius is 147.5 mm. The metal-emitting plate is a circular aluminum plate with a radius of 150 mm and a thickness of 1.8 mm; its edge is connected to the outside via an annular rubber ring of 1-mm thickness and 160-mm outer radius. The outermost side of the rubber ring is fixed (clamped) to simulate the structural support boundary conditions in the actual assembly.

In the multiphysics coupling setup, the metal emitting plate is modeled using the solid mechanics and magnetic field modules to simulate its elastic response under electromagnetic forces (with material properties of aluminum alloy). The surrounding air domain is modeled with the pressure acoustics module to solve for sound wave propagation and radiation. The coil is modeled with the magnetic field module to simulate the transient magnetic field and induction effects under the discharge current. To realistically reproduce the electromagnetic pulse source's drive process, an electrical circuit module is also incorporated to couple the coil with external circuit components (capacitor, resistor, etc.). In the circuit, the discharge capacitance is set to C_0, the initial charging voltage to U_0, and the loop resistance to R_0. The capacitor's discharge drives the coil to generate a strong pulsed current, which in turn induces eddy currents and electromagnetic force in the plate via electromagnetic induction, thus realizing coupled energy transfer among the electrical, magnetic, structural, and acoustic fields.

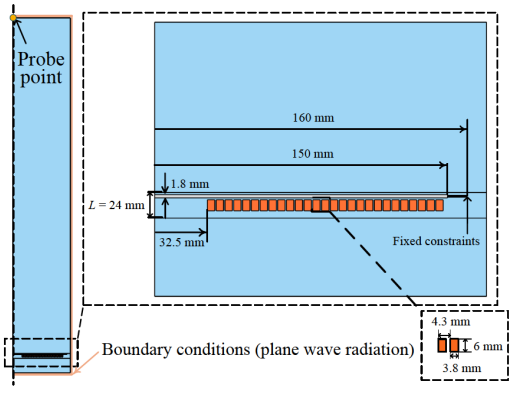


Fig. 2 2D axisymmetric model of an airborne acoustic electromagnetic pulse source.

2.1 Discharge circuit analysis

Assuming a discharge capacitance C_0 and circuit resistance R_0, and considering that the coil has its own inductance and a mutual inductance exists between the coil and the metal plate, the circuit equation during discharge can be written as[42]

$$(R_0 + R_c)I_c + \left(\frac{\mathrm{d}(L_c I_c)}{\mathrm{d}t} + \frac{\mathrm{d}(MI_w)}{\mathrm{d}t}\right) = U_c, \tag{1}$$

$$U_c = U_0 - \frac{1}{C_0}\int_0^t I_c \mathrm{d}t, \tag{2}$$

$$R_w I_w + \frac{\mathrm{d}(L_w I_w)}{\mathrm{d}t} + \frac{\mathrm{d}(MI_c)}{\mathrm{d}t} = 0, \tag{3}$$

where I_c represents the coil current, I_w is the equivalent eddy current induced in the metal plate, R_c is the coil's resistance, L_c is the coil's equivalent inductance, M is the mutual inductance between the coil and the plate, R_w and L_w are the equivalent resistance and self-inductance of the plate, respectively, and U_c is the instantaneous capacitor voltage. During the discharge process, the equivalent inductance of the coupled system and the total effective resistance jointly determine the rate of change of the current and the system's energy dissipation. The mutual inductance term reflects the electromagnetic coupling strength between the plate and coil, and its magnitude directly affects the amplitude of the induced eddy current. Thus, given the coil's structure and the plate's geometry, factors such as the capacitor's initial voltage U_0, the capacitance C_0, and the circuit resistance R_0 will directly influence the coil current's amplitude and waveform characteristics, thereby modulating the system's electromagnetic excitation strength and subsequent structural response.

Figure 3 shows the current evolution curves generated by the model under different capacitances and initial voltage conditions. The current pulse acts as the initial driving signal, and its characteristics directly affect the evolution of subsequent parameters. When the capacitor discharges, the current rapidly surges to a peak and then gradually decays. At the same voltage, as the capacitance increases, the current pulse width increases significantly. This is because the capacitance value determines the amount of charge stored in the capacitor, i.e., the larger the capacitance, the longer the discharge duration. For example, at 600 V, increasing the capacitance from 40 μF to 80 μF extends the current pulse duration from 0.38 ms to 0.57 ms. Additionally, when the capacitance is fixed, raising the initial voltage markedly increases the peak current. According to Ohm's law, given a roughly constant circuit resistance, the current peak is proportional to the voltage. For instance, for a given capacitance (C_0 = 80 μF), increasing the voltage from 600 V to 1000 V raises the current peak from 1.05 kA to 1.75 kA, with a faster rise and more rapid decay of the pulse. This shows that the charging voltage has a significant impact on the current's magnitude and dynamic characteristics.

When the discharge current flows through the pancake

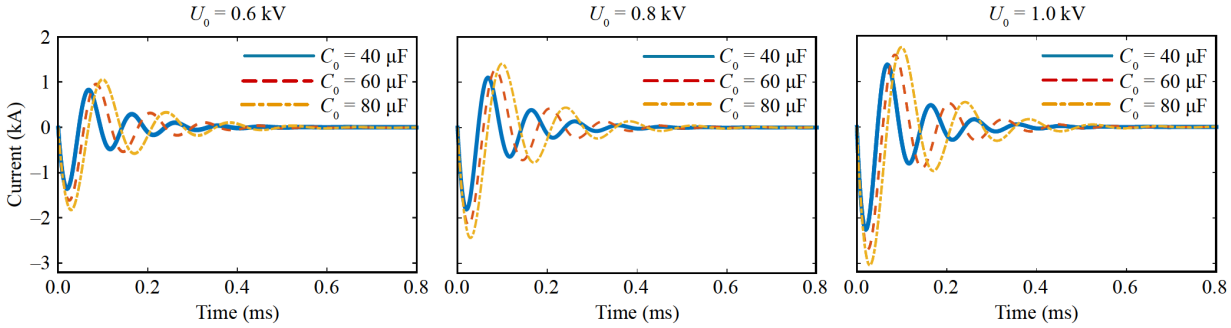


Fig. 3 Current values generated by the model under different capacitances and voltage values.

coil, the coil generates a pulsed magnetic field. According to Maxwell's equations, the governing relationships among the magnetic field intensity, current density, and magnetic flux density can be written as

$$\nabla \times \mathbf{H} = \mathbf{J}, \tag{4}$$

$$\nabla \times \mathbf{E} = -\frac{\partial \mathbf{B}}{\partial t}, \tag{5}$$

$$\nabla \times \mathbf{B} = 0, \tag{6}$$

$$\mathbf{J}_c = \frac{\mathbf{I}_c}{s}, \tag{7}$$

$$\mathbf{J} = \sigma_e \mathbf{E}, \tag{8}$$

where $\mathbf{H}$ is the magnetic field intensity, $\mathbf{J}$ is the current density of the metal plate, $\mathbf{B}$ is the magnetic flux density, $\mathbf{J}_c$ is the current density of the coil, and $\mathbf{E}$ is the electric field intensity; s is the cross-sectional area of the coil conductor, and σ_e is its electrical conductivity. ∇ denotes the vector differential operator (nabla operator). In Eqs. (4) and (5), it represents the curl operator, while in Eq. (6), it represents the divergence operator.

Based on the above electromagnetic equations, one can derive the induced electric field intensity:

$$\mathbf{E} = -\nabla \varphi - \frac{\partial \mathbf{A}}{\partial t} + (\mathbf{v} \times \mathbf{B}). \tag{9}$$

According to Ohm's law, the current density can be further obtained as

$$\mathbf{J} = -\sigma_e \nabla \varphi - \sigma_e \frac{\partial \mathbf{A}}{\partial t} + \sigma_e \mathbf{v} \times (\nabla \times \mathbf{A}), \tag{10}$$

where φ is the scalar potential, $\mathbf{A}$ is the magnetic vector potential, and $\mathbf{v}$ is the velocity of the medium. For the metal plate and air domains, the scalar potential term is neglected.

Combining the expression for current density with Ampère's circuital law, one can solve for the eddy current density $\mathbf{J}_e$ and the electromagnetic force density $\mathbf{f}_m$ acting on the plate[42]:

$$\mathbf{J}_e = -\sigma_e \frac{\partial \mathbf{A}}{\partial t} + \sigma_e \mathbf{v} \times \mathbf{B}, \tag{11}$$

$$\mathbf{f}_m = \mathbf{J}_e \times \mathbf{B}. \tag{12}$$

From the above analysis, it is evident that the coil current generates a magnetic field whose strength is proportional to the current. The magnetic field, in turn, induces eddy currents in the metal plate, and these eddy currents in the magnetic field are subject to the Lorentz force, producing an electromagnetic force that drives the metal plate's vibration. The vibration characteristics of the emitting plate are primarily determined by this electromagnetic force, which in turn is governed by the discharge capacitance C_0, the discharge voltage U_0, and the circuit resistance R_0.

In the present model, the acoustic radiation behavior of the metal-emitting plate under electromagnetic excitation is approximated as an axially symmetric piston source. Under far-field conditions, the acoustic radiation is predominantly governed by the overall normal vibration of the plate surface. Therefore, the radial and tangential components of the electromagnetic force are neglected, and only the axial component along the plate's normal direction is considered. Accordingly, the distribution of the axial component of the electromagnetic force density under axisymmetric conditions is derived, which represents the effective driving force responsible for the vibration of the plate. The axial electromagnetic force density is

$$f_{mz} = -J_{e\theta} B_r, \tag{13}$$

where $J_{e\theta}$ is the circumferential component of the eddy current in the plate, and B_r is the radial component of the magnetic field.

Under axisymmetric conditions in cylindrical coordinates (r, θ, z), the eddy current density has only a circumferential component. On this basis, the force density at each node of the metal plate can be calculated and integrated to obtain the total electromagnetic force acting on the plate:

$$F = \iiint f_{mz} \mathrm{d}V = \int_0^{2\pi} \int_0^R \int_0^h f_{mz} r \mathrm{d}r \mathrm{d}z \mathrm{d}\theta, \tag{14}$$

where R and h denote the radius and thickness of the plate, respectively. The electromagnetic force is treated as a body force distributed within the plate volume.

Figure 4 illustrates the variation of the total electromagnetic force over time under different capacitance and voltage conditions. The electromagnetic force is the direct source term driving the metal plate's vibration, and its

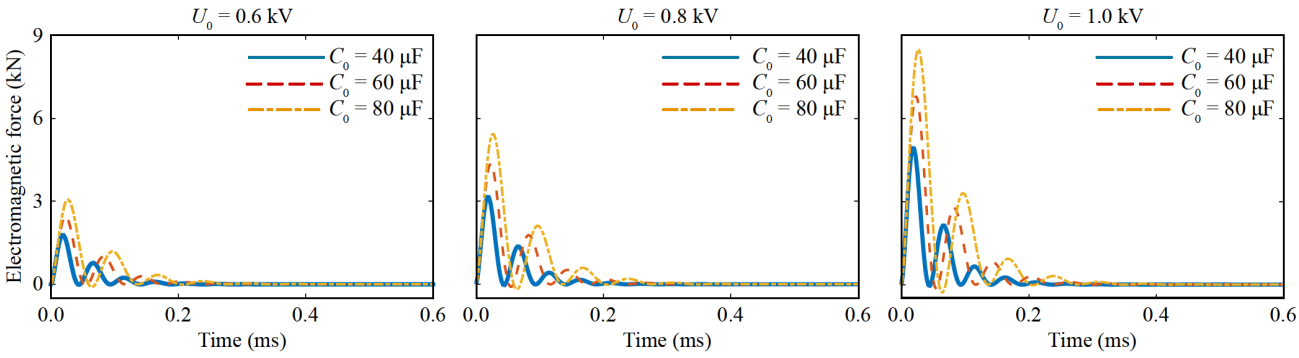


Fig. 4 Electromagnetic force generated by the model under different capacitances and voltage values.

strength directly determines the source's excitation efficiency and radiation performance. From Fig. 4, it can be seen that the electromagnetic force curves in all cases exhibit a typical pulsed shape. This arises from the transient nature of the discharge current: when a high-voltage capacitor releases current through the coil, the transient magnetic field induces eddy currents in the metal plate, and the interaction between them produces a strong axial repulsive electromagnetic force. Comparing the curves at different voltages reveals that, with the capacitance fixed, the capacitor's initial voltage is the dominant factor determining the peak value of the electromagnetic force. As the voltage is increased from 0.6 kV to 1.0 kV, the peak electromagnetic force is significantly enhanced. This is because the current peak is approximately proportional to the charging voltage under the given circuit parameters, and the electromagnetic force is proportional to the square of the current; therefore, the force peak grows roughly with the square of the voltage. For example, increasing the voltage to 1.67 times its original value (from 0.6 kV to 1.0 kV) causes the peak electromagnetic force to rise to about 2.8 times its original value, demonstrating a quadratic growth trend with voltage.

2.2 Structural-acoustic coupling model

Assuming a uniform distribution of electromagnetic force and neglecting any bending deformation of the plate, we treat the emitting plate together with the rubber ring as a single oscillator system with equivalent mass m_{eff}, stiffness k_{eff}, damping c_{eff}, and plate surface area A ($A = \pi a^2$). The system's equivalent single-degree-of-freedom dynamic equation can then be written as

$$m_{\text{eff}}x''(t) + c_{\text{eff}}x'(t) + k_{\text{eff}}x(t) = f_{\text{mz}}(t)A - p(t)A, \tag{15}$$

where $x(t)$ is the plate's equivalent normal displacement, $p(t)A$ is the acoustic reactive force (sound pressure) from the air, and $f_{\text{mz}}(t)A$ is the total electromagnetic thrust force.

The acoustic reaction force from the air can be represented using a radiation impedance model:

$$p(t)A = Z_{\text{rad}}V = \left[R_{\text{rad}} + \mathrm{i}\omega M_{\text{add}}\right](\mathrm{i}\omega x), \tag{16}$$

where R_{rad} is the radiation damping (corresponding to energy loss due to sound radiation) and M_{add} is the added mass (representing the inertial loading of the air). Substituting this into the motion equation above yields the classic coupled mass-spring model for acoustic radiation and structure:

$$\left[-\omega^2(m_{\text{eff}} + M_{\text{add}}) + \mathrm{i}\omega(c_{\text{eff}} + R_{\text{rad}}) + k_{\text{eff}}\right]x = F_{\text{em}}(\omega), \tag{17}$$

where $F_{\text{em}}(\omega)$ is the Fourier transform of the electromagnetic driving force. This model shows that the system's total effective mass ($m_{\text{eff}} + M_{\text{add}}$) is composed of the structure's equivalent mass plus the added mass introduced by the air load, and the total effective damping ($c_{\text{eff}} + R_{\text{rad}}$) comes from the structure's internal damping combined with the radiation damping resulting from acoustic energy radiation. This coupled model clearly reveals the physical mechanism by which the air load influences the plate's vibration characteristics through inertial and dissipative effects, providing a direct theoretical basis for analyzing the system's frequency response.

In the air domain, the sound pressure satisfies the acoustic wave equation along with continuity conditions for velocity and stress at boundaries:

$$\nabla^2 p - \frac{1}{c^2}\frac{\partial^2 p}{\partial t^2} = 0, \quad \mathbf{x} = (r, z),\ z > 0, \tag{18}$$

$$\begin{aligned} &v_n(\mathbf{x}_\Gamma, t) = \frac{\partial x(r,t)}{\partial t}, \\ &\rho_0\frac{\partial v_n}{\partial t} = -\frac{\partial p}{\partial n} \Rightarrow \rho_0\frac{\partial^2 x(r,t)}{\partial t^2} = -\left.\frac{\partial p}{\partial z}\right|_{z=0^+}, \end{aligned} \tag{19}$$

where c represents the sound speed in air, $\mathbf{x}$ is the position vector (with radial and axial components), and $v_n(\mathbf{x}_\Gamma, t)$ denotes the normal velocity on the boundary.

The above analysis indicates that the acoustic radiation capability of the emitting plate is determined by its own material density and area, as well as the electromagnetic force it experiences. For a given plate density and area, the electromagnetic force is jointly influenced by the capacitor's initial voltage U_0 and capacitance C_0 (Fig. 4).

Figure 5 shows the axial (on-axis) sound pressure responses over time at a distance of 1 m under various capacitance and

voltage excitation conditions. The sound pressure is a key indicator of the source's radiation efficiency, reflecting the ability to convert electromagnetic energy into acoustic energy.

From Fig. 5, the sound pressure signal exhibits a typical single-pulse waveform, which is consistent with the transient excitation characteristic of the electromagnetic pulse source. As the capacitance or the charging voltage increases, both the peak sound pressure and the radiated acoustic energy are enhanced. Further comparison shows that, under the same voltage conditions, increasing the capacitance does not significantly alter the peak current but prolongs the discharge duration, thereby extending the duration of the electromagnetic force and increasing the total impulse applied to the emitting plate. This results in higher acoustic energy radiation and more pronounced low-frequency components in the sound pressure signal. Under the same capacitance conditions, increasing the charging voltage leads to a nearly linear increase in the peak current, causing the peak electromagnetic force to scale approximately with the square of the voltage, which in turn produces a substantial increase in the radiated sound pressure amplitude.

In addition to these amplitude variations, the radiated sound pressure signals exhibit a distinct two-stage temporal structure, consisting of an initial high-frequency, low-amplitude component followed by a dominant low-frequency, large-amplitude component. The early-time high-frequency response is primarily associated with the rapid rise of the electromagnetic force during the capacitor discharge process, which excites higher-order and more localized structural vibration modes of the emitting plate. These modes decay rapidly and contribute mainly to the short-duration high-frequency component. The subsequent low-frequency response originates from the dominant low-order vibration modes of the emitting plate, which couple more efficiently with the surrounding air and therefore govern the main acoustic radiation and energy output of the source.

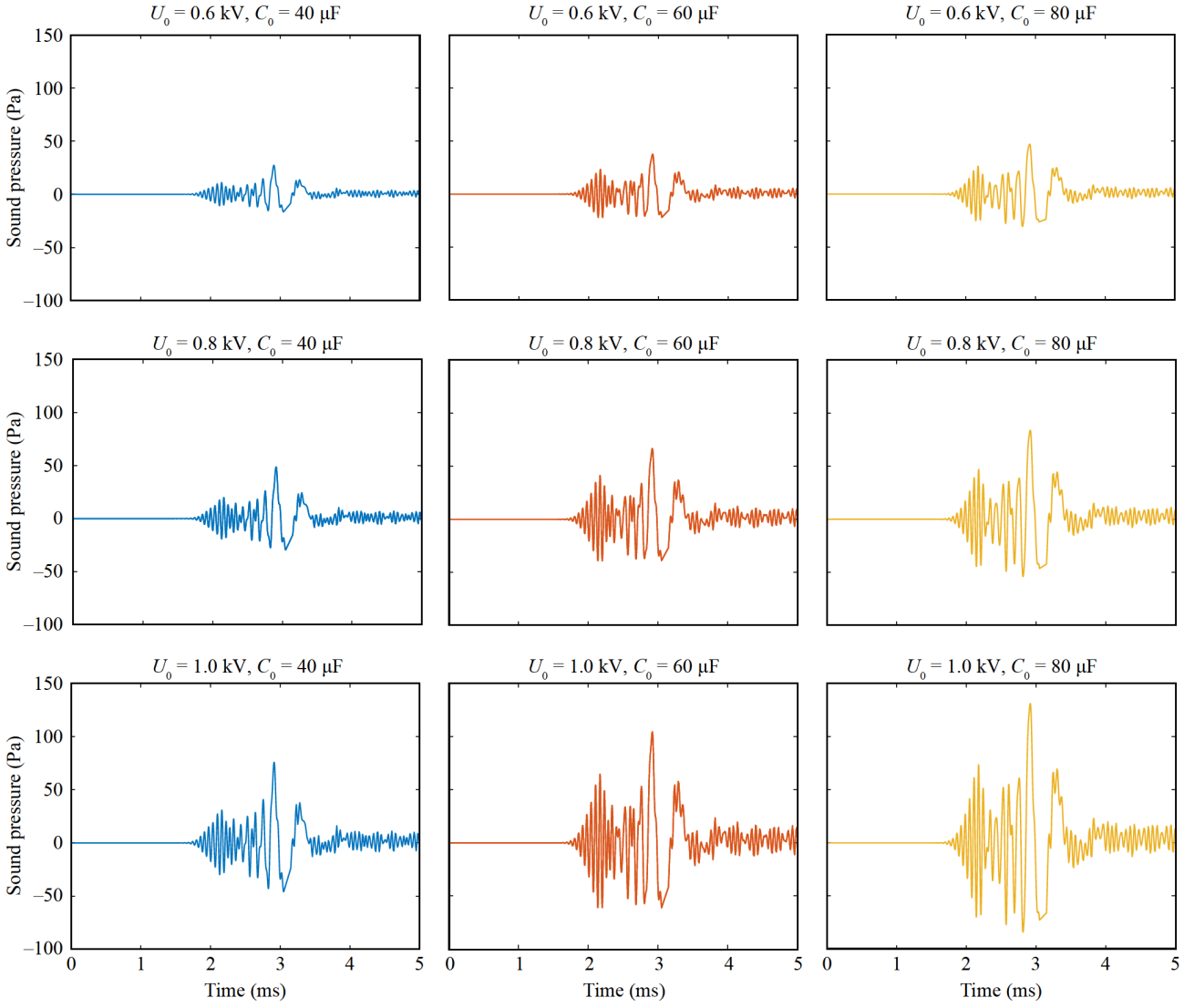


Fig. 5 Acoustic pressure signals under various excitation conditions.

In summary, the capacitance mainly influences the duration and energy distribution of the acoustic pulse, whereas the charging voltage predominantly controls the peak intensity of the radiated sound pressure. Together, these two parameters determine the transient radiation characteristics and overall acoustic performance of the electromagnetic pulse source in air.

Based on the above theoretical formulation, a four-physics coupled transient finite-element model is constructed to numerically investigate the electromagnetic excitation, structural vibration, and acoustic radiation processes.

2.3 Multiphysics coupling strategy and numerical implementation

Based on the geometric configuration and physical interfaces described above, a fully coupled transient finite-element model is established in COMSOL Multiphysics to investigate the electromagnetic excitation, structural vibration, and acoustic radiation processes of the electromagnetic pulse sound source. The model integrates the circuit, magnetic fields, solid mechanics, and pressure acoustics interfaces within a unified time-dependent framework, ensuring physical consistency along the energy transfer chain from electrical discharge to acoustic radiation.

The electrical discharge process is described using the circuit interface. The capacitor is initially charged to the voltage U_0, and the subsequent discharge loop is solved to obtain the time-dependent current $I_c(t)$ flowing through the pancake coil. This transient current $I_c(t)$ waveform serves as the excitation input to the electromagnetic model. The electromagnetic response is resolved using an axisymmetric magnetic field interface. The coil is modeled as a current-driven conductor excited by $I_c(t)$, while the emitting plate is treated as a conductive solid in which eddy currents with density $\mathbf{J}_e$ are induced by the time-varying magnetic field $\mathbf{B}$. Based on the computed magnetic flux density and eddy current density, the electromagnetic force density $\mathbf{f}_m$ acting on the emitting plate is evaluated within the electromagnetic formulation.

The structural response of the emitting plate is described using an axisymmetric solid mechanics interface with a linear elastic material model. The outer edge of the plate is constrained by fixed boundary conditions to represent the practical mechanical support, while the remaining regions are free to deform. The electromagnetic force density $\mathbf{f}_m$ obtained from the electromagnetic analysis is automatically transferred, through magneto-mechanical coupling, as a distributed body load to the structural model, thereby driving the transient elastic vibration of the emitting plate, which is characterized by the normal displacement $x(t)$ as defined in the theoretical formulation.

The surrounding air domain is modeled using an axisymmetric transient pressure acoustics interface, in which air is assumed to be a linear and lossless acoustic medium. The coupling between the structural and acoustic domains is realized at the solid-air interface via an acoustic-structure boundary condition. In this coupling, the normal velocity of the vibrating plate surface, given by the time derivative of the equivalent structural displacement $\partial x/\partial t$ and the corresponding normal acceleration $\partial^2 x/\partial t^2$ from the structural transient analysis, is imposed as the acoustic boundary excitation. This treatment enforces kinematic continuity at the solid-air interface and enables the calculation of the transient acoustic pressure response $p(t)$ associated with the vibrating plate.

A time-dependent solver is employed to capture the strongly coupled transient response of the system. An implicit generalized-α integration scheme is adopted, as it is well suited for multiphysics problems involving rapid electromagnetic excitation and structural-acoustic interactions, and provides controlled numerical dissipation of nonphysical high-frequency components. Automatic time stepping is used, with a sufficiently small initial time step to accurately resolve the sharp rise of the discharge current and the associated electromagnetic force. A time-step sensitivity analysis was conducted to confirm that further refinement of the time step does not lead to noticeable changes in the predicted sound pressure responses, thereby ensuring numerical stability and convergence.

To approximate an unbounded acoustic environment, plane wave radiation boundary conditions are applied at the outer boundaries of the air domain. Although this boundary condition is strictly non-reflective only for normally incident plane waves, the computational domain is chosen sufficiently large such that reflected waves from the outer boundaries do not reach the region of interest within the simulated time window. In addition, comparative simulations using alternative radiation boundary treatments were performed to assess the influence of the boundary condition. These comparisons confirm that the adopted radiation boundary condition is adequate for capturing the dominant radiation behavior and relative performance trends considered in this study. Any limitations associated with this approximation, therefore, do not affect the main conclusions of the work.

3 Investigation of the matching layer's operating mechanism

With the multiphysics model validated and the baseline radiation behavior established, the focus is now on addressing the key engineering challenge of impedance mismatch

through the introduction of a matching layer. To enhance the acoustic energy radiation efficiency of the electromagnetic pulse source in air, a homogeneous acoustic impedance matching layer (IML) is introduced on the outer surface of the metal emitting plate. The goal is to alleviate the pronounced impedance mismatch between the plate and air, achieving a gradual impedance transition at the solid–air interface and thereby improving the effective radiation of acoustic energy. In the simulation model, the capacitor is initially set to a certain capacitance $C_0 = 80$ μF and charged to a given voltage $U_0 = 1.0$ kV. During the modeling process, to balance computational efficiency with physical accuracy, a two-step modeling strategy is adopted: first, a circuit-electromagnetic-structural coupled model is constructed to simulate the transient electromagnetic force distribution generated when the capacitor discharges through the coil, obtaining the electromagnetic excitation load on the plate at various time instants; next, this electromagnetic force result is used as an external load in a structural–acoustic coupling model to further solve for the sound waves radiated by the plate in air. This strategy avoids the high computational cost of a fully coupled model and improves modeling efficiency while ensuring simulation accuracy. The structural–acoustic coupling model configuration is shown in Fig. 6.

Consider an acoustic transmission system composed of the emitting plate, an impedance matching layer, and the surrounding air, with characteristic acoustic impedances Z_1, Z_2, and Z_3, respectively, and matching layer thickness L. Under the assumption of 1D plane wave propagation, the sound intensity transmission coefficient through a single matching layer can be expressed as

$$t = \frac{4Z_1Z_3}{(Z_1+Z_3)^2\cos^2 kL + \left(Z_2+\frac{Z_1Z_3}{Z_2}\right)^2 \sin^2 kL}, \tag{20}$$

where k is the acoustic wavenumber in the matching layer.

When the matching layer impedance satisfies $Z_2 = \sqrt{Z_1Z_3}$ and the layer thickness satisfies the quarter-wavelength condition $L = \lambda/4$, the transmission coefficient reaches its theoretical maximum ($t = 1$), indicating optimal acoustic transmission. Accordingly, the target acoustic impedance of the matching layer is given by the geometric mean of the impedances of the emitting plate and air, which is approximately 8.53×10^4 Rayl (1 Rayl = 10 Pa s/m) in the present system.

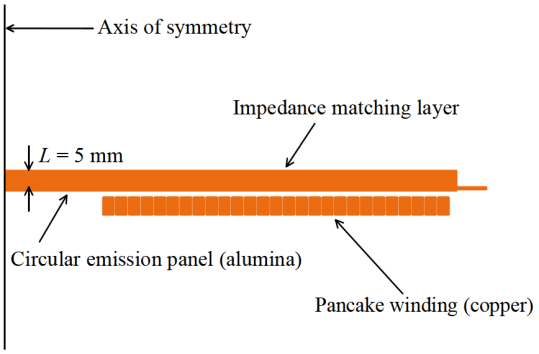


Fig. 6 2D axially symmetric geometric structure of the electromagnetic pulse acoustic source with an attached matching layer.

For a quarter-wavelength matching layer, the acoustic wave speed c is related to the layer thickness and target frequency by $c = 4Lf$. Taking the dominant radiation frequency of the source without a matching layer as approximately 4.2 kHz and selecting $L = 5$ mm, the corresponding reference values of the matching layer parameters are obtained as $c \approx 84$ m/s and $\rho \approx 1015$ kg/m^3. These values serve as baseline parameters for subsequent optimization and performance comparison.

Given that in practice the matching layer will vibrate together with the plate and exhibit significant structural-acoustic modal coupling behavior, the traditional quarter-wavelength theory may not accurately describe its dynamic response. Therefore, to further enhance the radiation performance of the source, a GA is employed to optimize the key parameters of the matching layer. The optimization variables are the longitudinal wave speed c and density ρ of the homogenized matching layer. The objective (fitness) function of the GA is defined as the maximum absolute value of the transient acoustic pressure measured at an on-axis observation point located 1 m above the source, which can be mathematically expressed as

$$\text{fitness} = \max_{t\in[0,T]} \left| p(r = 0, z = 1\ \text{m}, t) \right|, \tag{21}$$

where $p(r = 0, z = 1\ \text{m}, t)$ denotes the time-dependent acoustic pressure at the observation point, and T is the total simulation time window.

In the optimization process, the GA is directly coupled with the transient multiphysics finite-element model through the COMSOL-MATLAB LiveLink interface. For each individual in the GA population, the design variables (c, ρ) are automatically assigned to the COMSOL model, and a full transient multiphysics simulation is executed. Upon completion of the simulation, the peak axial sound pressure is extracted from the computed acoustic time history and returned to MATLAB as the fitness value for the GA. This procedure is repeated iteratively for all individuals and generations. The GA parameters are set as follows: a population size of 20, a maximum of 100 generations, and an elite retention strategy to ensure population diversity and robust global convergence. The optimal matching layer parameters obtained were a sound speed of 254.32 m/s and a density of 156.36 kg/m^3.

Simulation results (Fig. 7) show that introducing the

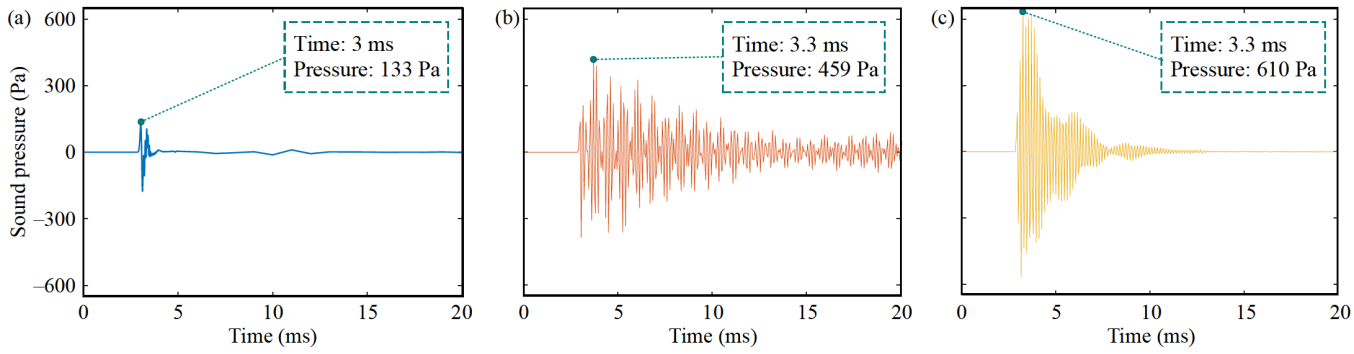


Fig. 7 Time-domain response of sound pressure at detection points under different matching layer structures: (a) Without matching layer; (b) With 1/4-wavelength theoretical parameter matching layer; (c) With genetically algorithm-optimized parameter matching layer.

quarter-wavelength matching layer significantly enhances the acoustic radiation capability of the system. The peak sound pressure at the 1 m axial detection point increases from 133 Pa in the no-layer case to 459 Pa with the baseline $\lambda/4$ matching layer. Frequency-domain analysis (Fig. 8) further reveals that the baseline structure exhibits two dominant spectral peaks at approximately 5 and 12 kHz, indicating that the acoustic energy radiation is distributed over multiple modes.

The lower-frequency peak around 5 kHz can be regarded as the primary standing-wave response near the design frequency (4.2 kHz), with its frequency slightly shifted upward due to structural-acoustic coupling effects. The higher-frequency peak near 12 kHz is attributed to a higher-order cavity resonance mode formed within the matching layer (e.g., a $3\lambda/4$ mode), whose frequency is close to a high-order eigenfrequency of the matching layer under compressional wave propagation conditions.

It should be noted that the quarter-wavelength matching layer is designed based on an idealized 1D transmission model, which provides a baseline matching condition at the target frequency. However, after the matching layer is introduced, the overall dynamic behavior of the system is governed by the coupled vibration of the emitting plate, the matching layer, and the surrounding air. The matching layer introduces additional effective mass and compliance,

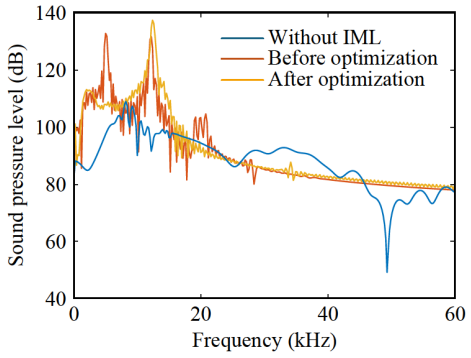


Fig. 8 The sound pressure levels obtained by performing FFT on the three time-domain sound pressures mentioned above.

which modifies the system's resonance characteristics and shifts the dominant radiation frequencies. Moreover, while the quarter-wavelength condition maximizes the local transmission coefficient at the interface, it does not necessarily maximize the global radiated acoustic energy of the coupled structural-acoustic system. Under transient broadband electromagnetic excitation, the radiated acoustic energy is dominated by frequencies at which the coupled system exhibits the highest vibration–radiation efficiency. As a result, the frequency corresponding to the maximum transmitted acoustic energy may deviate from the nominal quarter-wavelength design frequency.

With the genetically optimized matching layer, the peak sound pressure is further increased to 610 Pa, demonstrating a more pronounced enhancement in acoustic radiation performance. Frequency-domain results show that the sound pressure level around 12 kHz reaches approximately 137 dB, which is significantly higher than that of the baseline matching layer, while the main low-frequency peak shifts to around 2 kHz with a sound pressure level of about 113 dB. Overall, the optimized structure exhibits a spectral distribution characterized by enhanced high-frequency radiation and a flattened low-frequency response.

Notably, compared with the no-layer configuration, both the baseline and optimized matching layers substantially improve the system's low-frequency acoustic radiation capability. This behavior indicates that the role of the matching layer extends beyond simple frequency-selective cavity resonance and fundamentally alters the system's modal structure through dynamic coupling with the emitting plate. This spectral reconfiguration effect can be attributed to the combined action of the inertia loading effect and the elastic cavity effect introduced by the matching layer, that is, an inertia-cavity synergistic coupling effect between the emitting plate and the matching layer.

When a layer of acoustic impedance matching medium, i.e., a fluid layer with thickness L, density ρ, and sound speed c, is snugly attached to the outside of the emitting plate, the plate and the matching layer form a coupled vibration system.

From a mechanical-acoustic equivalent modeling perspective, this coupled system can be interpreted using a reduced-order lumped-parameter model, in which the emitting plate together with the matching layer provides an effective inertia, while the compressible medium inside the matching layer introduces an effective elastic stiffness. Specifically, during vibration, the fluid within the matching layer moves together with the plate, producing an added inertia effect[43]. At the same time, owing to the finite thickness and compressibility of the layer, sound waves undergo multiple reflections and interferences inside the matching layer, leading to the formation of a standing-wave field along the thickness direction.

This behavior is equivalent to an acoustic resonant cavity that is rigidly closed at one end (the emitting plate) and open at the other end (the air interface). When the thickness of the matching layer approaches a quarter of the acoustic wavelength, the cavity resonance becomes particularly pronounced, giving rise to a velocity node and a pressure antinode within the layer. This standing-wave resonance promotes the accumulation of acoustic energy inside the cavity and enhances the outward radiation efficiency. Consequently, the matching layer not only serves to smooth the acoustic impedance transition between the plate and air, but together with the emitting plate forms a strongly coupled mass-cavity system that significantly alters the vibration and radiation characteristics of the overall system.

In the low-frequency range, the fluid within the matching layer moves almost rigidly and in phase with the emitting plate, and its primary effect manifests as an added inertial load on the plate. The effective inertia of the coupled system can be approximated as $M = m_{\text{eff}} + m_2$, where $m_2 \approx \rho AL$ represents the effective mass contribution of the matching layer. Owing to this increase in effective mass, the natural frequency of the system decreases from its original value $f_0 \approx \sqrt{k_{\text{eff}} / m_{\text{eff}}} / 2\pi$ to a lower value $f_1 \approx \sqrt{k_{\text{eff}} / M} / 2\pi$. This added-mass effect leads to a downward shift of the resonance frequency. In this frequency range, the system response is dominated by inertia and corresponds to a mass-controlled regime, which is consistent with the dominant low-frequency acoustic energy component observed in the finite element method (FEM) spectra.

As the frequency increases, the motion of the matching layer gradually deviates from that of the emitting plate. Due to its finite thickness and compressibility, sound waves within the matching layer undergo multiple reflections and interferences, giving rise to a pronounced standing-wave field along the thickness direction. When the thickness of the matching layer approaches the quarter-wavelength condition, the layer can be equivalently regarded as an acoustic cavity that is rigidly closed at one end (the emitting plate) and open at the other end (the air interface). In this case, the primary role of the matching layer shifts from providing added inertia to supplying an effective elastic stiffness. The effective cavity stiffness can be approximated as $K_{\text{cav}} \approx \gamma P_0 A^2 / V_{\text{cav}}$, where P_0 is the ambient static pressure and V_{cav} denotes the effective cavity volume inside the matching layer.

In this high-frequency range, the system response becomes dominated by the cavity stiffness, entering a cavity-controlled regime. The matching layer no longer behaves as a purely transmissive medium, but rather acts as an active resonant unit with its own vibrational degree of freedom. Through the boundary coupling conditions of velocity continuity and pressure balance, a strong bidirectional interaction is established between the matching layer and the emitting plate. This cavity resonance not only leads to a local accumulation of acoustic energy within the matching layer but also exerts a reactive force on the plate, thereby significantly modifying the dynamic response of the plate and giving rise to high-frequency resonance peaks in the radiation spectrum. The physical origin and ordering of these peaks are consistent with those observed in the FEM results.

It should be emphasized that the purpose of this reduced-order model is not to predict the exact resonance frequencies of the coupled system, but rather to elucidate the underlying physical mechanisms governing the transition from inertia-dominated behavior at low frequencies to cavity-dominated behavior at higher frequencies. Although geometric non-uniformities and distributed effects are neglected in this simplified representation, the model provides a quantitative framework that explains the formation mechanisms and relative distribution of the dominant resonance peaks observed in the numerical simulations, thereby supporting the proposed inertial-cavity synergistic coupling mechanism.

In the case without a matching layer (Fig. 9(a)), the propagation of sound waves in air is severely limited: the sound pressure amplitude is overall low, the sound field's color map is faint, the axial wavefront structure is fragmented, and the radiation directivity is poor, which reflects the strong reflections and low coupling efficiency caused by the impedance mismatch. In the optimized matching layer case (Fig. 9(c)), the sound field distribution is further strengthened: the sound pressure amplitude is significantly higher, the wavefront is flatter and more continuous, and the radiation efficiency is greater. Compared to the $\lambda/4$ matching structure, the optimized structure exhibits higher stability of energy output in the time domain and achieves a more pronounced focusing of the sound beam in space.

In summary, a properly designed matching layer is decisive in increasing the sound wave amplitude, improving wavefront propagation characteristics, and enhancing radiation efficiency. In particular, a parameter optimization based on the system's coupled dynamics offers greater practicality and engineering value than traditional $\lambda/4$ matching.

It should be noted that the optimized density ρ and sound speed c obtained from the GA do not correspond to a single specific bulk material. Instead, they represent target effective

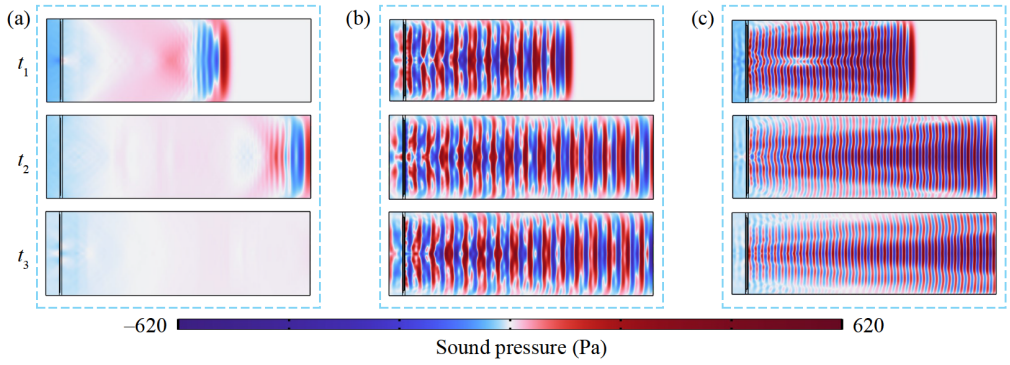


Fig. 9 Acoustic field distributions at three typical time points (t_1 = 2 ms, t_2 = 3 ms, and t_3 = 4 ms): (a) Without matching layer; (b) With 1/4-wavelength matching layer; (c) With optimized parameter matching layer.

acoustic parameters for the homogenized matching layer. During the optimization process, the search ranges of density and wave speed were restricted to values that are physically achievable by lightweight porous materials, polymer foams, or architected metamaterials. Therefore, the optimized parameters should be interpreted as physically feasible design targets, which serve as reference values for the microstructural design of the matching layer presented in the following section, rather than as purely mathematical optima without physical meaning.

4 Optimized design of the pentamode material matching layer microstructure

In the above discussions, we investigated the operating mechanism of the impedance matching layer without considering the layer's microstructure. In this work, the matching layer is implemented using a pentamode material structure. The unit cell geometry of the pentamode material is shown in Fig. 10(a), and its geometric parameters are illustrated in Fig. 10(b). The primary parameters include the unit cell side length l, the wall thickness t, and the width w and length h of the added mass block. The base material of the structure is epoxy resin, with a density of 1186 kg/m^3, Young's modulus of 3.20 GPa, and Poisson's ratio of 0.37. The equivalent longitudinal wave velocity of the pentamode material is mainly determined by the cell wall thickness t, while the equivalent density is mainly determined by the mass of the cell's central mass block (w, h). To characterize the modal properties of the pentamode unit cell and verify its fluid-like behavior, the dispersion relation for a typical microstructure, with unit cell side length l of 6.93 mm, t of 0.0585 mm, w of 0.1018 mm, and h of 0.3973 mm, is shown in Fig. 10(d), where the red solid line represents the pentamode material's longitudinal mode, the light blue solid line represents the shear mode, and the green solid line represents the rotational (torsional) mode. It can be seen that the shear mode is significantly suppressed over the frequency range of interest, indicating that the pentamode microstructure exhibits a dominant compressional response. It should be emphasized that the band structure analysis is not intended to describe wave propagation through the finite-thickness matching layer in the radiation direction, but rather to verify the pentamode nature of the unit cell, namely the suppression of shear modes and the validity of treating the material as an

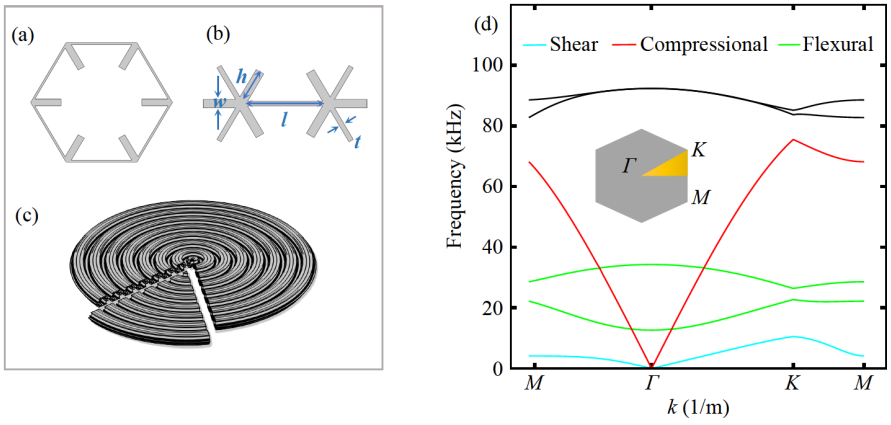


Fig. 10 The parameters and band structure of the pentamode unit cell: (a) Unit cell geometry; (b) Structural parameters; (c) 3D schematic of the unit cell; (d) Dispersion curves of the pentamode metamaterial used in this work.

effective fluid. Under this condition, shear resonances in the matching layer are greatly suppressed. Figure 10(c) shows a 3D schematic of the pentamode material matching layer.

The pentamode matching layer was designed to have a thickness of 12 mm. Using the classical quarter-wavelength matching theory, the required effective acoustic wave speed and density were determined, and in combination with a band-structure retrieval method[33,34], the microstructural parameters were selected to construct the pentamode matching layer model. In this matching layer, the shear modes are strongly suppressed, thereby effectively achieving impedance matching under near-fluid behavior. Figure 11 shows the 2D axisymmetric model geometry of the electromagnetic pulse source with the pentamode matching layer included.

It should be noted that in practical applications, the pentamode matching layer still faces two important challenges. First, there is significant dynamic coupling between the matching layer and the emitting plate. Because the pentamode material's elastic response is influenced by the plate's motion, the coupling between the plate and the matching layer will directly alter the matching layer's local acoustic field distribution and dynamic boundary conditions, thereby introducing nonlinear disturbances to its impedance matching performance. Second, in this study, the matching layer structure is designed with only a single layer ofunit cells of finite thickness, whereas the equivalent medium parameters for pentamode materials are derived under the Bloch periodic assumption, using dispersion relations and band structures. Such an equivalent model is strictly applicable to an infinite or periodically repeated structure; in a finite single-layer scenario, its mechanical behavior may deviate from the idealized equivalent response, leading to shifts or degradation in impedance matching performance. In summary, the triple coupling among the plate, matching layer, and air, as well as the finite-periodicity (scale) effects, are key factors that influence the actual working performance of the pentamode matching layer. These factors should be further considered and corrected in future optimization designs and modeling.

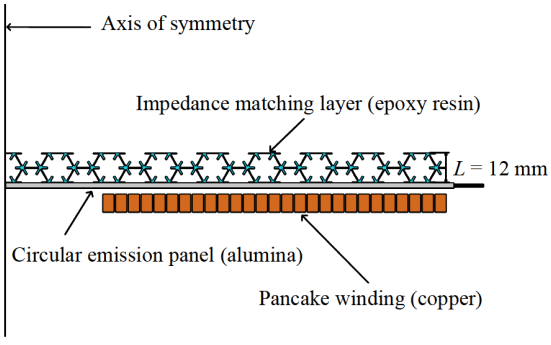


Fig. 11 2D axially symmetric geometric structure of the electromagnetic pulse acoustic source with pentamode metamaterial (PM) matching layer.

The GA is further employed to optimize the microstructural parameters of the pentamode matching layer. The optimization variables include the unit-cell wall thickness t and the mass block width and length (w, h). The same fitness function defined in Sec. 3 (Eq. (21)) is adopted for the optimization of the pentamode microstructural parameters, i.e., the maximum absolute value of the transient axial sound pressure measured at a detection point located 1 m away from the source.

In the optimization process, the GA is directly coupled with the transient multiphysics finite-element model through the COMSOL-MATLAB LiveLink interface. For each individual in the GA population, the microstructural parameters (t, w, h) are automatically assigned to the COMSOL model, and a full transient multiphysics simulation is performed. Upon completion of the simulation, the peak axial sound pressure is extracted from the computed acoustic time history and returned to MATLAB as the fitness value for the GA. This procedure is repeated iteratively for all individuals and generations.

The GA parameters are set as follows: a population size of 20, a maximum of 100 generations, and an elite retention strategy to improve convergence stability and global search capability. The optimization workflow is illustrated in Fig. 12. Table 1 compares the pentamode unit cell's geometric parameters and effective properties before and after the GA optimization.

To evaluate the influence of different matching strategies on acoustic radiation performance, we carried out time-domain simulations for three representative cases: no matching layer, with a quarter-wavelength theoretical matching layer, and with the GA-optimized pentamode matching layer. The corresponding time-domain sound pressure responses at 1 m on the axis are shown in Fig. 13.

In the absence of a matching layer (Fig. 13(a)), the peak sound pressure is 133 Pa and the overall radiation efficiency is low. After adding a traditional $\lambda/4$ pentamode matching layer (Fig. 13(b)), the peak sound pressure is slightly increased to 147 Pa, indicating that it improves the impedance transition between the plate and air to a certain extent. In contrast, after incorporating the GA-optimized pentamode matching layer (Fig. 13(c)), the peak sound pressure is dramatically increased to 584 Pa, which is over four times higher than that with no matching layer, demonstrating that the proposed structure possesses excellent acoustic radiation capability and impedance matching performance under coupled conditions.

Through fast Fourier transform (FFT) analysis of the time-domain signals (Fig. 14), one can see that the optimized matching layer (yellow curve) achieves higher sound pressure levels over most frequencies compared to both the no-layer case (blue curve) and the quarter-wavelength pentamode matching layer case (red curve), demonstrating that the

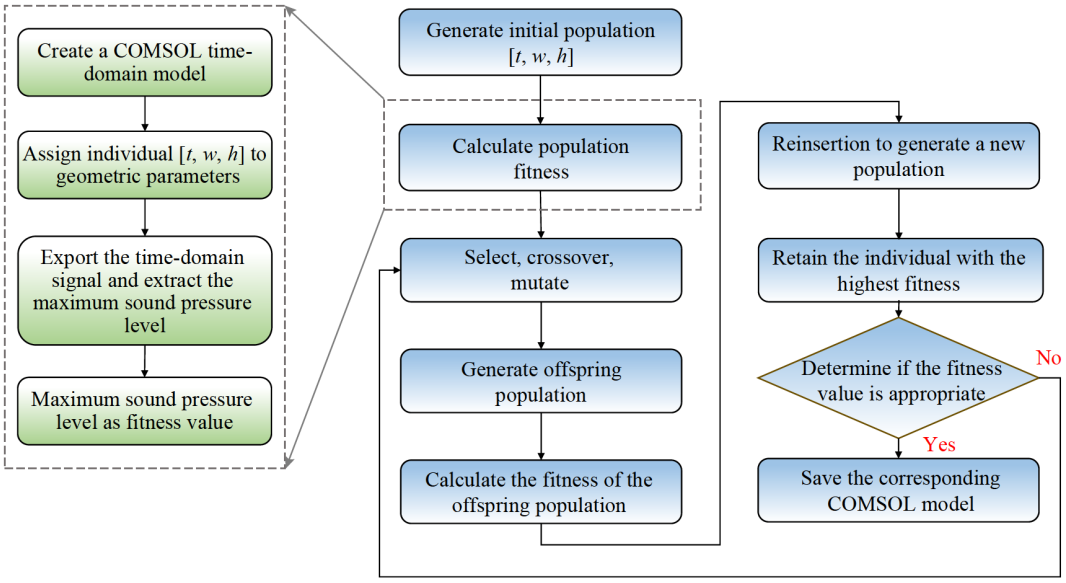


Fig. 12 Flowchart of the GA-based optimization process for the pentamode matching layer design.

Table 1 Geometric parameters and effective characteristics of the pentamode unit cell

	c_{eff}	ρ_{eff}	t (mm)	w (mm)	h (mm)
Before optimization	192.05	444.27	0.1085	0.2918	0.3973
After optimization	77.514	289.63	0.0585	0.1018	0.3973

optimization strategy has overall enhanced the matching layer's radiation efficiency. Additionally, after adding a matching layer, multiple peaks appear in the frequency-domain response. This can be attributed to a more complex inertial-cavity coupling mechanism between the matching layer and the plate. This mechanism includes the influence of the matching layer as added mass on the system's resonance frequencies, as well as the matching layer's role as an elastic acoustic cavity that vibrates relative to the plate and couples with it.

Specifically, with the unoptimized matching layer, the frequency response shows multiple resonance peaks at around 2, 14, and 16 kHz. The peak at 2 kHz corresponds to the downward shift of the fundamental mode due to the added mass effect: the presence of the matching layer significantly increases the system's total mass, thereby lowering the first resonance frequency. The high-frequency peaks at 14 and 16 kHz arise from the cavity resonance characteristics of the matching layer. Its equivalent stiffness together with its equivalent mass forms independent higher-order resonant modes. These frequency features exemplify the inertial-resonant cavity coupling mechanism between the plate and the matching layer, wherein the matching layer not only acts as an added load affecting the overall system dynamics, but also participates in the resonance as an independent acoustic resonator.

In the GA-optimized configuration, the redistribution of resonance peaks reflects a modified inertial–cavity coupling condition. The peak near 4 kHz corresponds to an enhanced primary resonance governed predominantly by the effective inertia of the coupled system, while the additional peak appearing around 10 kHz indicates a transition regime in which the inertial and cavity effects are both significant. This mid-frequency peak reflects a strengthened coupling between the

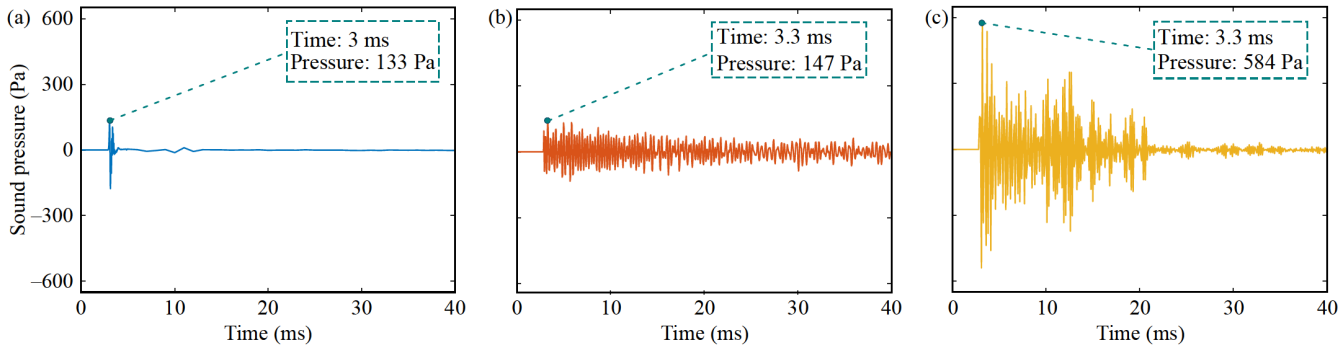


Fig. 13 Time-domain sound pressure responses at 1 m axial distance under three different matching conditions: (a) No matching layer; (b) Quarter-wavelength PM matching layer; (c) Optimized PM matching layer.

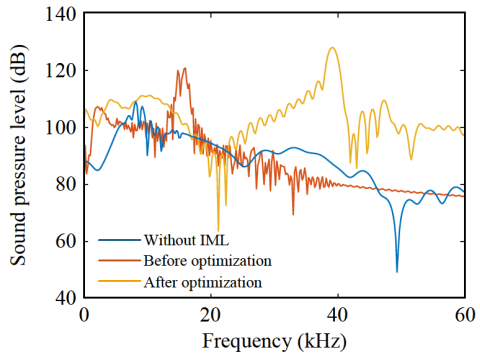


Fig. 14 Sound pressure level at different conditions.

emitting plate and the matching layer, leading to improved energy exchange between structural vibration and acoustic radiation. Furthermore, the pronounced high-frequency peak at approximately 39 kHz indicates a strongly enhanced cavity-controlled response. Although the low-frequency peak is relatively moderate in amplitude, its broader bandwidth and elevated sound pressure level demonstrate improved energy coupling in the mass-controlled regime. Overall, these results demonstrate that the genetic optimization strategy effectively tailors the inertial-cavity synergistic coupling, thereby enhancing acoustic radiation performance across low-, mid-, and high-frequency bands.

Figure 15 shows the acoustic field distributions at 2, 3, and 4 ms for three structural configurations: without any matching layer, with the quarter-wavelength theory-based matching layer, and with the optimized matching layer. The introduction of a matching layer has a significant impact on the sound radiation characteristics and propagation behavior. In the case without a matching layer (Fig. 15(a)), the sound pressure magnitudes are generally low, i.e., the color scale is mostly pale, and the axial wavefronts are indistinct and broken, indicating the presence of a severe impedance mismatch—most of the acoustic energy is reflected or rapidly dissipated at the plate-air interface, and the radiation efficiency is low. With the quarter-wavelength matching layer added (Fig. 15(b)), the sound pressure amplitude increases noticeably, the sound field exhibits richer color gradients, and the wavefront structure becomes clearer and more orderly. However, some wavefront bending and beam spreading phenomena still occur locally, which means the matching performance has not reached an optimum.

In contrast, the model with the GA-optimized matching layer (Fig. 15(c)) demonstrates the best sound field performance at each time instant: the sound pressure amplitude is maximized, the color scale is much more saturated, and the wavefront maintains good axial symmetry and continuity during propagation, with energy distribution that is tightly focused. This superior radiation behavior indicates that optimizing the pentamode structure's parameters, while fully accounting for multiphysics coupling mechanisms, can effectively improve the quality of the impedance match at the interface, suppress energy reflection and scattering losses, and thereby significantly boost the electromagnetic pulse source's acoustic radiation efficiency and field intensity uniformity in air.

This analysis of the sound field is consistent with the earlier time-domain and frequency-domain observations, which indirectly verify the effectiveness and engineering applicability of the proposed pentamode matching layer in enhancing the source's radiation performance.

It should be noted that the findings presented in this study are primarily based on numerical simulations. While the coupled electromagnetic–structural–acoustic finite-element framework provides detailed insight into the operating mechanisms of the electromagnetic pulse sound source, independent validation is essential for further confirmation.

Several potential validation strategies can be considered in future work. First, simplified experimental prototypes of the electromagnetic pulse source with interchangeable matching layers could be fabricated, allowing direct measurement of transient sound pressure and comparison with simulation predictions under controlled excitation conditions. Second, intermediate-level validation may be achieved by comparing reduced-order analytical models, such as simplified single-degree-of-freedom structural–acoustic models, with the full

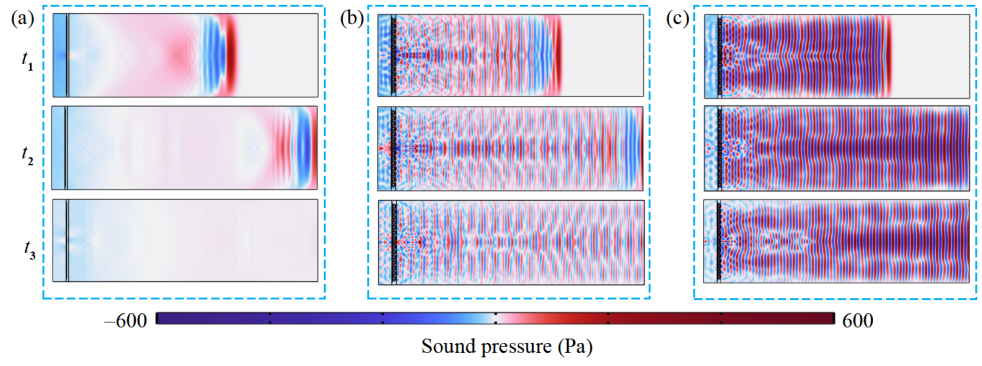


Fig. 15 Acoustic field distributions at three typical time points (2, 3, and 4 ms): (a) Without any matching layer; (b) With the unoptimized matching layer; (c) With the optimized matching layer.

multiphysics simulation results to verify consistency in trends and dominant response characteristics. Third, component-level validation can be performed by independently characterizing the electromagnetic force, structural vibration, and acoustic radiation subsystems, thereby assessing the accuracy of each coupled interface within the numerical model.

These validation strategies provide feasible pathways to further substantiate the numerical findings reported in this work and will be pursued in future studies.

5 Mechanical reliability and manufacturability assessment

To address practical concerns regarding the manufacturability and mechanical robustness of the proposed pentamode matching layer, a supplementary assessment was conducted, with a particular focus on fabrication feasibility and transient structural integrity under electromagnetic impact loading.

Regarding manufacturability, recent advances in high-resolution polymer additive manufacturing have demonstrated the feasibility of fabricating polymer-based micro-lattice and architected structures with characteristic feature sizes well below 100 μm. In particular, projection micro-stereolithography (PμSL)[44] has been widely applied to the fabrication of mechanically functional polymer microstructures with feature sizes and wall thicknesses on the order of several tens of micrometers, exhibiting sufficient geometric fidelity for engineering applications. In parallel, recent developments in two-photon polymerization (2PP) have further extended the achievable fabrication resolution into the micro- and nanoscale regime[45]. Consequently, the optimized microstructural wall thickness of 0.0585 mm obtained in this study lies well within the demonstrated capabilities of current state-of-the-art polymer micro-fabrication technologies, indicating the practical manufacturability of the proposed matching layer design.

To evaluate mechanical reliability, a transient structural analysis was performed using a commercial finite element solver. The time-dependent Lorentz force derived from the electromagnetic simulations was applied as an equivalent dynamic load on the matching layer. Considering the brittle nature of epoxy-based photopolymers, the maximum principal stress was adopted as the failure criterion. The analysis focused on the structural response under a 1 kV discharge condition, corresponding to the operating scenario investigated in the acoustic simulations. During the transient simulation, the maximum principal stress within the pentamode material region was monitored over time to identify the peak loading condition.

The simulation results indicate that the peak maximum principal stress in the epoxy matching layer reaches approximately 8 MPa during the transient loading process, with stress concentrations mainly occurring at the slender struts and junction regions of the pentamode microstructure. Compared with the tensile strength of epoxy materials reported in the literature, which typically lies in the range of 40–60 MPa depending on material formulation and fabrication conditions, the resulting safety factor exceeds 5 even when a conservative lower-bound strength value of 40 MPa is assumed. This confirms that the matching layer remains well within the elastic regime and maintains sufficient structural integrity under the investigated electromagnetic impact loading.

Overall, this supplementary analysis demonstrates that the optimized pentamode matching layer is not only acoustically effective, as discussed in the preceding sections, but also mechanically feasible and manufacturable using existing polymer micro-fabrication technologies. This assessment further supports the practical applicability of the proposed design for electromagnetic pulse acoustic sources operating in airborne environments.

6 Conclusion

In this paper, a design and optimization approach employing a pentamode material impedance matching layer was proposed and validated to address the impedance mismatch challenge of electromagnetic pulse acoustic sources operating in air. By establishing a coupled multiphysics model and applying a GA to optimize the matching layer parameters, the radiation performance of the electromagnetic pulse source was significantly enhanced. The results demonstrate that an appropriately designed matching layer can effectively smooth the impedance transition between the emitting plate and air, leading to a substantial increase in sound pressure output and energy transfer efficiency.

This study provides a viable pathway for enhancing the acoustic radiation intensity and efficiency of electromagnetic pulse sources in airborne environments, and lays a solid foundation for the optimized design and experimental investigation of similar pulse sound sources. In addition to the demonstrated acoustic and vibroacoustic performance improvements, supplementary assessments of manufacturability and mechanical reliability were conducted to support the practical applicability of the proposed pentamode matching layer. These assessments indicate that the optimized design is compatible with existing fabrication technologies and can maintain structural integrity under transient electromagnetic excitation, thereby reinforcing the engineering relevance of the proposed impedance matching strategy.

References

[1] Edgerton H E, Hayward G G. The “boomer” sonar source for seismic profiling. *J. Geophys. Res.*, 1964, **69**(14): 3033–3042

[2] Harrington P K, Moody C D. Deep-tow multi-purpose sparker system. Offshore Technology Conference, OTC, Houston, Texas, USA, 1976

[3] Ardus D A. The development of techniques for marine geological surveys. In: Teleki P G, Dobson M R, Moore J R, *et al*. (eds). Marine minerals: advances in research and resource assessment. Dordrecht, Netherlands: Springer Netherlands, 1987: 81–98

[4] Wood W T, Gettrust J F, Spychalski S E. A new deep-towed, multichannel seismic system. *Sea Technol.*, 2003, **44**(9): 44–47, 49

[5] Hamahashi M, Otsuka H, Suzuki Y, *et al*. Shallow structure and late Quaternary slip rate of the Osaka Bay fault, western Japan. *Prog. Earth Planet. Sci.*, 2024, **11**: 8

[6] Rebesco M, Camerlenghi A, De Santis L, *et al*. Seismic stratigraphy of Palmer Deep: a fault-bounded late Quaternary sediment trap on the inner continental shelf, Antarctic Peninsula Pacific margin. *Mar. Geol.*, 1998, **151**(1–4): 89–110

[7] Tsuchiya T, Kagawa Y, Okamuro T, *et al*. Finite element simulation of electromagnetic induction transducers for impulsive intense sound. *IEEE Trans. Ultrason. Ferroelectr. Freq. Control*, 1997, **44**(5): 1077–1086

[8] Müller C, Milkereit B, Bohlen T, *et al*. Towards high-resolution 3D marine seismic surveying using Boomer sources. *Geophys. Prospect.*, 2002, **50**(5): 517–526

[9] Monrigal O, de Jong I, Duarte H. An ultra-high-resolution 3D marine seismic system for detailed site investigation. *Near Surf. Geophys.*, 2017, **15**(4): 335–345

[10] Ditchburn R J, Burke S K, Posada M. Eddy-current nondestructive inspection with thin spiral coils: long cracks in steel. *J. Nondestr. Eval.*, 2003, **22**(2): 63–77

[11] Simpkin P G. The boomer sound source as a tool for shallow water geophysical exploration. *Mar. Geophys. Res.*, 2005, **26**(2): 171–181

[12] Jian X, Dixon S, Grattan K T V, *et al*. A model for pulsed Rayleigh wave and optimal EMAT design. *Sens. Actuators A Phys.*, 2006, **128**(2): 296–304

[13] Leng T, Li M X, Huang Z Y, *et al*. The research and design of the electromagnetic acoustic experiment system and the experiment research. *Acta Acust.*, 2009, **34**(5): 437–444 (in Chinese)

[14] Huang Y, Zhang L, Zhang X, *et al*. Electroacoustic process study of plasma sparker under different water depth. *IEEE J. Ocean. Eng.*, 2015, **40**(4): 947–956

[15] Mu Y S, Ji P F, Cai Y F, *et al*. Design and research on underwater electromagnetic pulse source with high intensity. *Acta Acust.*, 2015, **40**(2): 254–262 (in Chinese)

[16] Feng J, Wei J, Liu C C, *et al*. Complementarity analysis of parametric array and spark source sub-bottom profilers. *Mar. Geol. Front.*, 2019, **35**(9): 63–68

[17] Xie J X, Zhang Y L, Jiang M, *et al*. Principle research on pulsed sound source in deep sea based on high-power electromagnetic pulse. *J. Integr. Technol.*, 2021, **10**(2): 98–108

[18] Vesnaver A, Baradello L. A workflow for processing mono-channel Chirp and Boomer surveys. *Geophys. Prospect.*, 2023, **71**(8): 1387–1403

[19] Gao X, Zhou J, Xie H, *et al*. Discharge experiment and structure optimisation simulation of impulse sound source. *Energies*, 2024, **17**(18): 4565

[20] Du X, Zhou J, Gao X. Electroacoustic comparison and optimization of low-power impulse sound-source needle series electrodes. *Energies*, 2025, **18**(13): 3230

[21] Jiang B, Zheng J L, Huang X X, *et al*. Experimental study on deep sea broadband electromagnetic pulse sound source based on pressure compensation balance. *J. Integr. Technol.*, 2025, **14**(3): 134–144

[22] Velikhov E P, Panchenko V P. Large-scale geophysical surveys of the earth’s crust using high-power electromagnetic pulses. In: Mikada H, Zhdanov M S, Kasahara J (eds). Active geophysical monitoring. 3rd ed. New York: Elsevier, 2025: 5–25

[23] Zhou P, Jia H, Bi Y, *et al*. Water–air acoustic communication based on broadband impedance matching. *Appl. Phys. Lett.*, 2023, **123**(19): 191701

[24] Wang C, Wang C, Liu N, *et al*. Optimize multilayer matching layer design for tone-burst underwater acoustic transducers. *J. Acoust. Soc. Am.*, 2022, **152**(3): 1942–1950

[25] Bakhtiary Yekta H, Norris A N. A broadband solid impedance transformer for acoustic transmission between water and air. *J. Sound Vib.*, 2025, **598**: 119120

[26] Norris A N. Acoustic metafluids. *J. Acoust. Soc. Am.*, 2009, **125**(2): 839–849

[27] Zhou C, Li Q, Sun X, *et al*. Two-dimensional pentamode metamaterials: properties, manufacturing, and applications. *Crystals*, 2024, **14**(6): 521

[28] Cushing C W, Kelsten M J, Su X, *et al*. Design and characterization of a three-dimensional anisotropic additively manufactured pentamode material. *J. Acoust. Soc. Am.*, 2022, **151**(1): 168–179

[29] Chu Y, Sun T, Wang Z, *et al*. Low-frequency broadband acoustic modulation mechanism of composite pentamode metamaterials. *Phys. Lett. A*, 2023, **491**: 129212

[30] Li G, Chen Y, He H. Design method and infeasibility criteria for honeycomb pentamode cloak. *Phys. Lett. A*, 2022, **442**: 128174

[31] Gong F, Li Q, Xiao Z, *et al*. Experimental verification of latticed acoustic metamaterials with pentamode to bandgap characteristics. *Eur. Phys. J. B*, 2024, **97**(12): 192

[32] Cai C, Tai T, Wang Q, *et al*. Research on the low frequency characteristics of anisotropic three-dimensional pentamode metamaterials. *Phys. Scr.*, 2025, **100**(10): 105537

[33] Chen Y, Liu X, Hu G. Latticed pentamode acoustic cloak. *Sci. Rep.*, 2015, **5**(1): 15745

[34] Sun Z, Zhao L, Yang J. Underwater acoustic self-focusing and bending in conformal Mikaelian lens by pentamode metafluid. *J. Phys. D: Appl. Phys.*, 2023, **56**(50): 505304

[35] Zhao A, Zhu Y, Lin Z, *et al*. Fatigue tolerant multifunctional pentamode materials with simultaneous acoustic invisibility and vibration isolation. *Thin-Walled Struct.*, 2025, **211**: 113174

[36] Cai C, He G, Yin Y, *et al*. Topological transmission of elastic waves on a macroscopic pentamode metamaterial plate. *J. Appl. Phys.*, 2023, **133**(23): 234901

[37] Ahmadzadeh F, Bahrami A, Zaremanesh M. Large-scale underwater acoustic cloak based on honeycomb lattice pentamode metamaterials. *Sci. Rep.*, 2025, **15**: 25623

[38] Li G, Tang L, Sorokin V, *et al*. CVAE-based inverse design of two-dimensional honeycomb pentamode metastructure for acoustic cloaking. *Thin-Walled Struct.*, 2025, **206**: 112623

[39] He L, Yang L, Cai X, *et al*. Composite pentamode metamaterials for enhanced wave manipulation by asymmetric surface structure. *Small Struct.*, 2025, **6**(9): 2500112

[40] Zhao S D, Wang Y S, Zhang C, *et al*. Topology-optimized reflection-type pentamode metasurfaces for broadband underwater beam regulation. *Wave Motion*, 2025, **135**: 103515

[41] Xu H, Sun Z, Zhao L, *et al*. Luneburg cloak with pentamode metafluid. *Wave Motion*, 2026, **143**: 103721

[42] Cao Q, Li L, Lai Z, *et al*. Dynamic analysis of electromagnetic sheet metal forming process using finite element method. *Int. J. Adv. Manuf. Technol.*, 2014, **74**(1): 361–368

[43] Brown J A, Sharma S, Leadbetter J, *et al*. Mass-spring matching layers for high-frequency ultrasound transducers: a new technique using vacuum deposition. *IEEE Trans. Ultrason. Ferroelectr. Freq. Control*, 2014, **61**(11): 1911–1921

[44] Ge Q, Li Z, Wang Z, *et al*. Projection micro-stereolithography based 3D printing and its applications. *Int. J. Extreme Manuf.*, 2020, **2**(2): 022004

[45] Basu P. Advancements in two-photon polymerization (2PP) for micro and nanoscale fabrication. *Nanomanufacturingf*, 2025, **6**(1): 1